An Expendable Microstructure Profiler for Deep Ocean Measurements

XIAODONG SHANG, YONGFENG QI,[a] GUIYING CHEN, AND CHANGRONG LIANG[a]

State Key Laboratory of Tropical Oceanography, South China Sea Institute of Oceanology, Chinese Academy of Sciences, Guangzhou, China

ROLF G. LUECK AND BRETT PRAIRIE

Rockland Scientific International Inc., Victoria, British Columbia, Canada

HUA LI

Oceanographic Research Laboratory, JFE Advantech Co., Ltd., Nishinomiya, Hyogo, Japan

(Manuscript received 8 April 2016, in final form 7 September 2016)

ABSTRACT

Measurements of turbulence in the deep ocean, particularly close to the bottom, are extremely sparse because of the difficulty and operational risk of obtaining deep profiles near the seafloor. A newly developed expendable instrument—the VMP-X (Vertical Microstructure Profiler–Expendable)—carries two microstructure shear probes to measure the fluctuations of vertical shear into the dissipation range and can profile down to a depth of 6000 m. Data from nine VMP-X profiles in the western Pacific Ocean near 11.6°N over rough topography display bottom-intensified turbulence with dissipation rates increasing by two factors of 10 to 4×10^{-9} W kg^{-1} within 200 m above the bottom. In contrast, over smooth topography in the southern South China Sea near 11°N, three profiles show that turbulence in the bottom boundary layer increases only slightly, with dissipation rates reaching 1×10^{-10} W kg^{-1}. The eddy diffusivity over rough topography reached to 5×10^{-3} m^2 s^{-1}. The average diffusivity over all depths was 0.3×10^{-4} and 0.9×10^{-4} m^2 s^{-1} for the tests in the southern South China Sea and in the western Pacific Ocean, respectively, and these values are much larger than previous estimates of less than $\approx 0.1 \times 10^{-4}$ m^2 s^{-1} for the main thermocline.

1. Introduction

The study of turbulent mixing in the ocean is very important for understanding the global ocean overturning circulation because of its influence on climate. Most of the turbulence measurements in the ocean suggest that the vertical eddy diffusivity is approximately 10^{-5} m^2 s^{-1} (Gregg 1989), which is a factor of 10 smaller than the canonical mean vertical eddy diffusivity (Munk 1966) that maintains the global thermohaline circulation. However, deep measurements are rare, and most profiles are shallower than 1000 m.

One possible reason for the discrepancy between the observed and predicted diffusivity is the lack of deep measurements. The distribution of diapycnal mixing is extremely inhomogeneous, varying with both depth and location (Kunze et al. 2006; Whalen et al. 2012). Near-bottom turbulence is driven by tides and geostrophic flows impinging on rough and sloping topography (Wunsch and Ferrari 2004; Nikurashin and Ferrari 2010). Some scientists (Toole et al. 1994; Polzin et al. 1997; Ledwell et al. 2000; Kunze et al. 2006; Waterhouse et al. 2014) found evidence of enhanced turbulent mixing in the deep ocean near the bottom, particularly in regions where the bottom is rough. For example, Polzin et al. (1997) reported diffusivities exceeding 5×10^{-4} m^2 s^{-1} for the bottommost 150 m above the Mid-Atlantic Ridge. Recently, Waterhouse et al. (2014) showed that the global-average diffusivity below 1000-m depth is $O(10^{-4})$ m^2 s^{-1} based on microstructure observations. However, this study does not include the benthic boundary layer. The energy to generate and maintain

Denotes Open Access content.

[a] Additional affiliation: University of Chinese Academy of Sciences, Beijing, China.

Corresponding author e-mail: Xiaodong Shang, xdshang@scsio.ac.cn

DOI: 10.1175/JTECH-D-16-0083.1

the benthic layer is thought to come from bottom friction (Fricker and Nepf 2000), the shoaling and critical reflection of high-wavenumber internal waves (Thorpe 1997), the interaction of ocean currents with rough topography, shear-induced convection (Lorke et al. 2005), and barotropic eddies. The height of the benthic bottom boundary layer can reach several tens of meters (Lentz and Trowbridge 1991). Numerous studies (Lueck and Mudge 1997; Ledwell et al. 2000; Garrett 2003) have demonstrated the occurrence of enhanced mixing up to several hundred meters above sloping bathymetry. Tracer measurements (Ledwell and Hickey 1995; Rye et al. 2012) have demonstrated the importance of bottom mixing for basin-scale transport processes. The bottom layer is a component of the circulation of abyssal waters and is one layer that is not resolved, or included, in most models of meridional circulation (Mashayek et al. 2015), partly because there have been very few microstructure measurements extending into the ocean bottom. The two deep turbulence profilers currently in operation—the High Resolution Profiler (HRP) and the Vertical Microstructure Profiler (VMP)-6000 (St. Laurent et al. 2012)—have profiled into the ocean bottom but have done so because of ballast release failures (and other technical faults) rather than by intent, which is extremely risky.

A new technology, developed by Rockland Scientific International Inc. and JFE Advantech Co., Ltd., to measure deep (up to 6000 m) ocean turbulence right to the bottom is described in section 2. Sample profiles taken with this new instrument in the western Pacific Ocean (wPO) over rough topography and in the southern South China Sea (sSCS) over smooth topography are presented in section 3. In section 4, full-depth profiles of the diapycnal diffusivity at these test sites are derived using the rate of dissipation of kinetic energy ε, taken with this instrument, and concurrent CTD profiles.

2. Instrumentation

The VMP–Expendable (VMP-X; Fig. 1) is a freely falling profiler that descends with a speed of 0.6–0.8 m s^{-1}. The profiler contains both a datalogger control unit and a nonrecoverable sensor package (MicroXM). The MicroXM communicates with the datalogger through an unprotected fiber-optic cable. The MicroXM is equipped with two shear probes (Osborn 1980) to measure turbulent fluctuations of horizontal velocity, and one thermistor to measure temperature and its vertical gradient. The MicroXM is attached to the VMP-X via a release system that allows it to separate from the VMP-X when the profiler reaches either a target depth or the seafloor. After releasing the MicroXM, the VMP-X rises to the surface at a speed of 1.0–1.2 m s^{-1}.

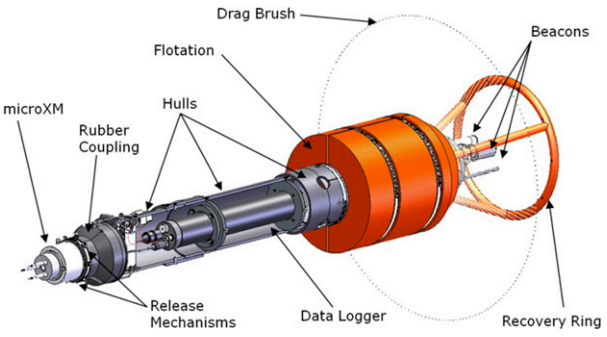

FIG. 1. Sectional view of the VMP-X.

a. VMP-X

The major components of the VMP-X system (Figs. 1 and 2) are the MicroXM at the bottom of the instrument, a rubber coupler, and release system that attaches the MicroXM to an acrylonitrile butadiene styrene (ABS) tube that forms a freely flooding hull. The top section of the hull is surrounded by a cylinder of syntactic foam. An aluminum recovery ring is attached to the top end of the hull, along with a radio beacon, a strobe light, and a combined GPS receiver and satellite transmitter. The datalogger and control unit are mounted inside the hull. All components are rated to a depth of 6000 m.

The datalogger is housed in a pressure case located within the ABS tube and below the flotation (Figs. 3). It records the data from the MicroXM and issues a release signal based on pressure, fall rate, and profile duration. The datalogger has three external connectors: An underwater optical feedthrough for connecting with the MicroXM; a 10-pin underwater connector for linking to a host computer, turning on the instrument and recharging the datalogger battery; and a two-pin underwater connector to energize the burn wire release cable. A 14.8-V rechargeable lithium-ion battery of 96-kJ capacity can energize the datalogger for up to 60 h.

The MicroXM is attached to the lower end of the VMP-X by a rubber coupler and a customized hose clamp. Mechanical vibrations are usually the main source of shear signal corruption (Moum and Lueck 1985), and the rubber coupler isolates the mechanical vibrations of the profiler from the MicroXM. The rear section of the VMP-X contains three pieces of flotation—two that combine to make the collar around the ABS tube and one inside the upper end of the tube. After a MicroXM is released upon the completion of a profile, the density of the profiler is reduced to

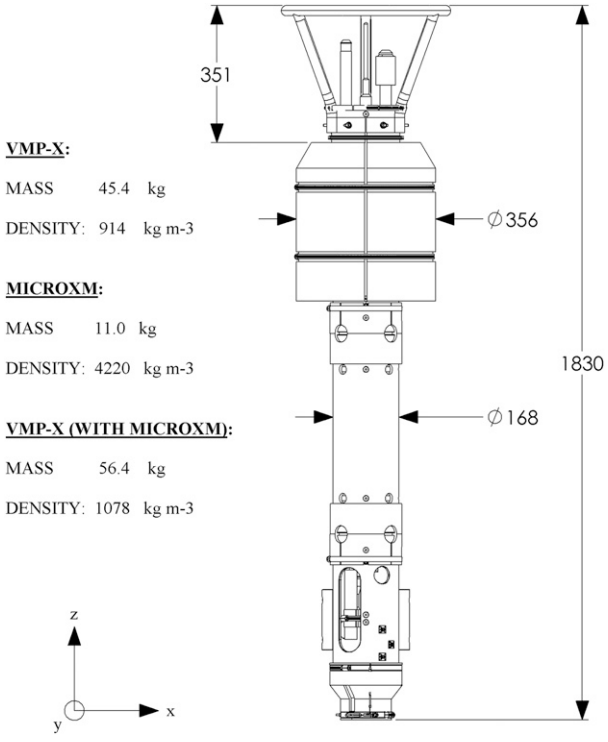

FIG. 2. Engineering drawing (mm) of the VMP-X without the MicroXM.

914 kg m^{-3}, giving it the buoyancy required to ascend to the ocean surface. Also located on the rear section of the VMP-X are three beacons for locating the instrument after it has returned to the surface. Once on the surface, an Iridium beacon transmits the GPS location to both a handheld Iridium receiver on the ship and a preassigned set of e-mail addresses. A VHF radio beacon transmits pulses that are used by a ship-based receiver to determine the direction to the VMP-X while it is within line of sight of the receiver. A light-emitting diode (LED) flasher operates at night to aid the recovery operation. All beacons are deactivated when the VMP-X is submerged. All are powered internally and operate independently.

b. *Release system*

The VMP-X is equipped with three release mechanisms. The primary mechanism is the burn wire release. Should the burn wire fail to release the MicroXM, there are two secondary release mechanisms. For deployments to less than 6000 m, the secondary release is the galvanic link release. For deployments where the bottom lies deeper than 6000 m, the secondary release mechanism is the rupture disk (RD) release.

The burn wire is a simple and effective sacrificial anode that upon disintegration by electrolysis will release the tension in the retaining hose clamp, allowing the MicroXM to slip out freely. Upon the trigger of a release signal, a positive electric potential (13–16 V via a 10Ω resistor) is applied to the burn wire, with respect to a cathode in contact with seawater, and the electrolysis disintegrates the burn wire, which frees the MicroXM. The burn wire is insulated from seawater except for a 3-mm section. The electrolysis is concentrated into this short and exposed section, and disintegrates the wire in 70–100 s. A release signal is triggered upon (i) hitting the ocean bottom, (ii) losing communication with the MicroXM continuously for more than 60 s, (iii) exceeding a selected depth, or (iv) exceeding a selected duration.

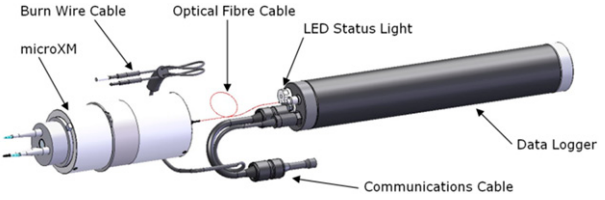

FIG. 3. MicroXM and datalogger and their interconnections.

The galvanic link release relies on the corrosion of a metal link that dissolves in seawater in 3.5–4.5 h at 2°C. It is usually disintegrated upon recovery of the VMP-X and is replaced for every deployment. The galvanic link release—like the burn wire release—is attached to the release clamp assembly located on the front of the rubber coupler.

The RD uses the hydrostatic pressure of the seawater to break a thin stainless steel diaphragm when the pressure exceeds 6000 dbar. The RD release is a secondary safety feature that is used when profiling in regions where the bottom depth exceeds 6000 m, such as over canyons and trenches, to protect the flotation from damage. The RD has a nominal burst pressure of 5998 dbar with a tolerance of +1.5%/−0.75% of the nominal burst pressure at 2°C. Therefore, the burst pressure range is 5950–6090 dbar at 2°C.

After a profile has been completed and the release mechanisms have freed the MicroXM, the optical fiber link to the VMP-X must be severed. Although the fiber is fairly strong under tension (it breaks at 40 N), its strength is greatly reduced under bending. Therefore, to sever the optical connection, the fiber is loosely tied using an overhand knot (Fig. 3) to induce a tight bend in the loop upon separation of the MicroXM from the VMP-X. The tension from either the weight of the MicroXM (in case the VMP-X is still falling) or the buoyancy force of the VMP-X (in case the VMP-X is on the bottom) is sufficient to break the tightly bent fiber.

c. *MicroXM*

The MicroXM is the nonrecoverable sensor portion of the instrument system. It contains a single electronics

TABLE 1. Sensors, signals, bandwidths (BW), and sampling rates (f_s) of the MicroXM. ADXL denotes the Analog Devices accelerometer.

Sensor	Signal	BW (Hz)	f_s (s^{-1})	Description
sh1	$\partial u/\partial z$	150	1250	x-axis shear probe
sh2	$\partial v/\partial z$	150	1250	y-axis shear probe
T	T	80	312.5	Thermistor without preemphasis
T_dT	$T + \partial T/\partial t$	150	1250	Thermistor with preemphasis
Ax	A_x	150	1250	x-axis piezoceramic vibration sensor
Ay	A_y	150	1250	y-axis piezoceramic vibration sensor
P	P	5	312.5	Keller pressure transducer without preemphasis
P_dP	$P + 20\partial P/\partial t$	5	312.5	Keller pressure transducer with preemphasis
Pitch	θ_x	5	312.5	x-axis ADXL103 inclinometer
V_Bat	V_B	0.3	312.5	Battery voltage

board that supports the analog processing of the signals from two shear probes, one thermistor, two vibration sensors, a pressure transducer, and a single-axis inclinometer (Table 1). The shear probes used on the MicroXM have the same tip geometry as the standard probes of Macoun and Lueck (2004, designated ''mantle''), but the supporting stem is shorter, wider, and fabricated from aluminum instead of stainless steel (Fig. 4). The shear probes are oriented to sense two orthogonal components of the fluctuation of horizontal velocity. The temperature sensor is fabricated from a model 25BB104N thermistor made by Amphenol, Inc., and is inserted into an aluminum sting of the same dimensions as the shear probes. This thermistor is insulated from seawater by a layer of glass but is otherwise unprotected from the ambient pressure. It is not as fast as the FP07 thermistor that is conventionally used for microstructure profiling, but neither thermistor model has a frequency response that is sufficient to resolve the full spectrum of temperature fluctuations at the profiling speed of the VMP-X (Sommer et al. 2013). The pressure transducer is a model PA10L, rated for 6000 dbar, manufactured by Keller, Inc. It is recessed into a hole in the center of the front bulkhead (Fig. 4). The two vibration sensors are fabricated by Rockland from piezoceramic benders, are embedded into the dry side of the front bulkhead, and are aligned to sense the components of acceleration along the axes of sensitivity of the shear probes. An inclinometer model ADXL103, made by Analog Devices, Inc., is soldered to the circuit board to measure the rotation of the MicroXM around its x axis. It has an accuracy of $\pm 1.5°$ and a much finer resolution.

All signals are low-pass filtered for antialiasing purposes and are sampled by a 16-bit analog-to-digital converter at signal-dependent slow and fast rates (Table 1). The sampled signals are transmitted to the datalogger over a single-mode unprotected fiber-optic link. The entire electronics of the MicroXM are energized by a series-connected pair of lithium CR123 batteries (nominally 6 V) that are soldered to the circuit board and can operate the MicroXM for up to 12 h. The typical duration of a 6000-dbar profile is 3 h. The series voltage of the CR123 batteries is also measured by the data sampler. The MicroXM is turned on by attaching a magnet to the side of its front bulkhead (Fig. 4).

d. Calibration

The calibration of the MicroXM consists of two parts: the signal conditioning electronics board and the sensors. The signal conditioning board is checked for its static characteristics, such as gain, using precision 0.01% resistors to calibrate the pressure and the temperature circuits. All circuit components that determine static gains are accurate to 0.1% and have temperature coefficients of less than $10 \times 10^{-6}\,K^{-1}$. The equivalent accuracies are 3 mK and 1 dbar for temperature and pressure, respectively.

The frequency-dependent gain of the shear, thermistor, and pressure circuits are determined by components with 2% accuracy with temperature coefficients of $\pm 100 \times 10^{-6}\,K^{-1}$. The frequency-dependent gains of these preemphasized signals are calibrated only for selected production samples of the boards. However, errors of more than ≈10% are detectable in the final noise check that is applied to all boards.

The thermistor temperature sensors are calibrated by measuring their resistance near 2°, 15°, 25°, and 35°C. These readings are regressed against the first-order Steinhart–Hart equation (Steinhart and Hart 1968), which is accurate to ±25 mK, over the oceanic range of temperature. The deviation is systematic and parabolic with a minimum in the center of the calibration range.

The pressure transducer is calibrated by its manufacturer (Keller, Inc.) to an accuracy of 0.1% and their voltage pressure coefficients are used to form a first-order polynomial relating raw data to pressure in physical units. A history of more than 200 recalibrations by Rockland of the type of transducer used with the VMP-X has demonstrated that the Keller calibrations are

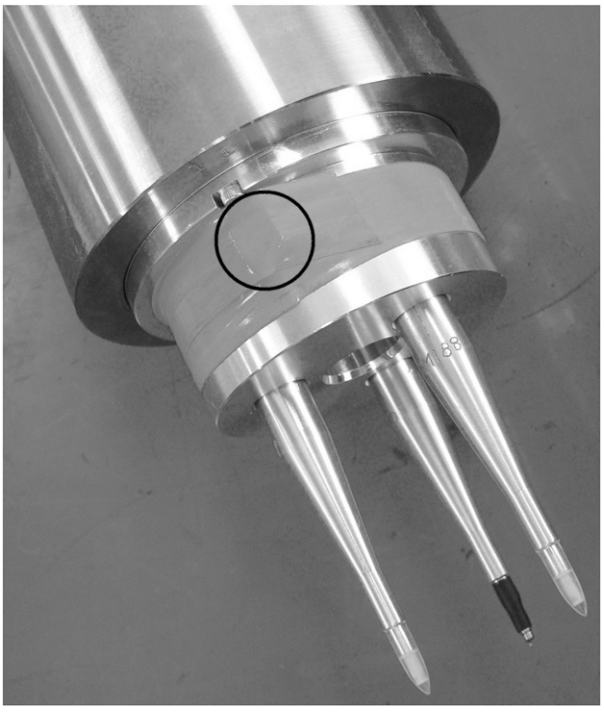

FIG. 4. Shear probes (white tips), thermistor (black band), and pressure transducer, which is recessed out of view at the center of the front bulkhead of the MicroXM. The black circle marks the on–off magnet, which is covered with tape.

within the stated specification but that the transducer output is better approximated by a second-order regression. A linear calibration has errors of up to ±50 dbar at a pressure of 6000 dbar.

The shear probes are calibrated by rotating them in a vertical jet with angles of attack of −6°, 0,° and 6° using the method of Osborn and Crawford (1980). The accuracy and repeatability is 5%. The inclinometer is calibrated by taking samples while its axis of sensitivity is aligned with and against gravity. The sum and difference of these readings, divided by 2, are the offset and sensitivity, respectively. These coefficients are accurate to better than 0.1%, but the zero point of the inclinometer is temperature dependent and this results in errors of up to ±1.5° over the oceanic temperature range. The temperature coefficient of sensitivity is unknown. The piezo-accelerometers that are used to sense vibrations are not calibrated.

3. Field tests

The field tests of the VMP-X were conducted in September 2014, using the Research Vessel *Shiyan 3*, in the southern South China Sea (sSCS), and in October 2015, using the Research Vessel *Kexue*, in the western Pacific Ocean (wPO). Three profiles were taken in the sSCS in the area of 10.0°–11.5°N, 111.5°–113.0°E, where the bottom is smooth and approximately 4000 m deep. Nine profiles were collected in the wPO in the region of 2.0°–11.5°N, 138.5°–143.5°E, where the bottom was rough and its depth ranges from 2500 to 6000 m. The VMP-X impacted the bottom and successfully released the MicroXM in all nine (three) profiles in the wPO (sSCS).

Here, we present two profiles: one taken in the sSCS at 11°N, 112.5°E (Fig. 5, red triangle) and the other collected in the wPO at 11.56°N, 138.86°E (blue triangle), in the region linking the Mariana and Yap Trenches. This passage is the only pathway for the exchange of deep seawater between the West and East Mariana Basins and the Caroline Basin. These two profiles were chosen because of their nearly identical latitude. During each VMP-X deployment, vertical profiles of finescale temperature and salinity were measured using a conductivity–temperature–depth (CTD) profiler, and finescale velocity shear variance was measured using a lowered acoustic Doppler current profiler (LADCP).

a. Pitch and fall rate of the VMP-X

For the profile in the sSCS, the VMP-X fell at 0.6 m s^{-1} near the surface and slowed to 0.57 m s^{-1} at the

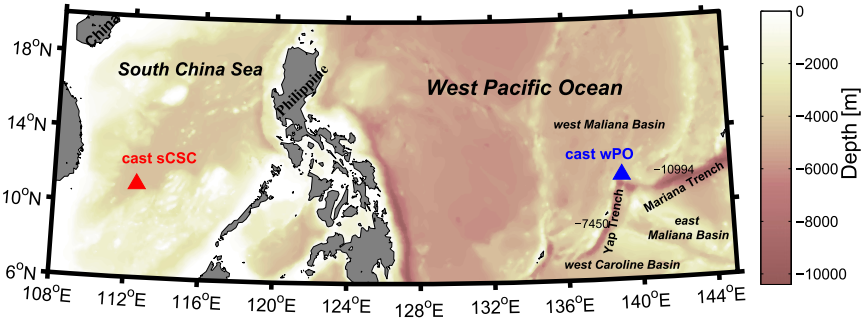

FIG. 5. Chart of the wPO and the SCS with depth shading. Red (blue) triangle marks the locations of the test profile in the sSCS (wPO).

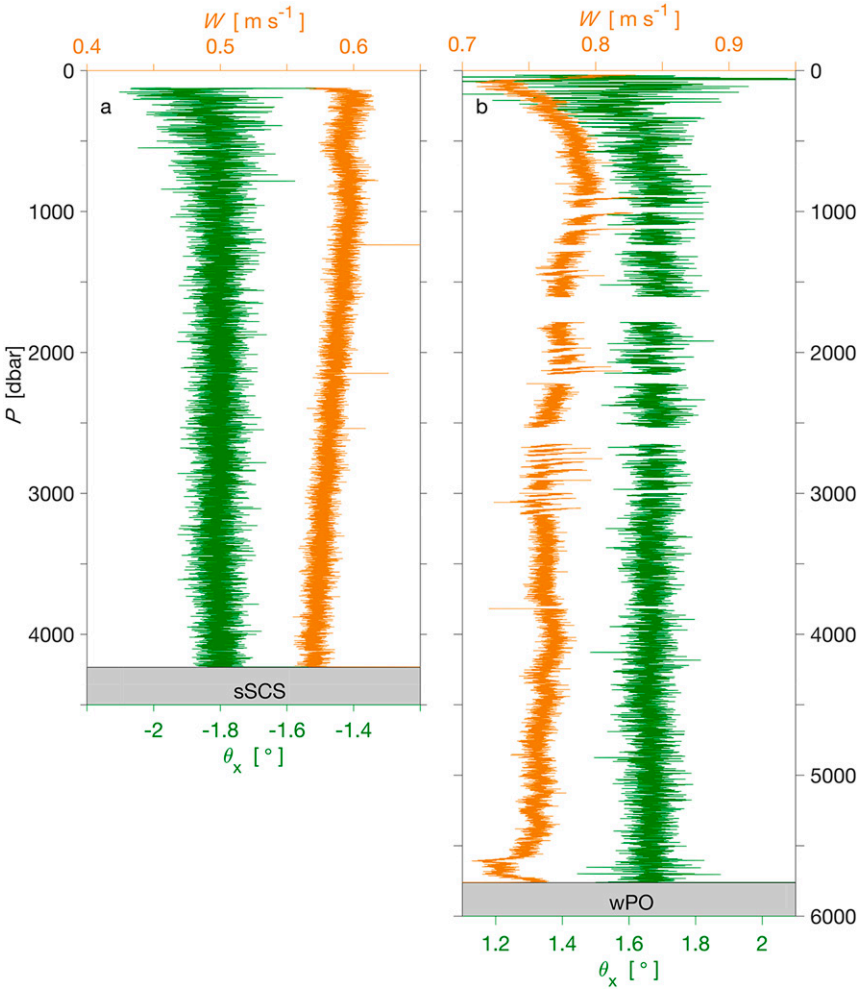

FIG. 6. Profiles of the pitch (green) and fall rate (gold) of the VMP-X for the (a) sSCS and (b) wPO. Gray shading identifies the bottom.

bottom (Fig. 6a, gold) due to the increasing density of seawater with depth. The typical pitch angle was −1.8° (Fig. 6a, green) and it fluctuated by ±0.05° below 1000-m depth and slightly more when the VMP-X was shallower. The length scale of the fluctuations is about 5 m. The large-scale shift of pitch during the first 1000 m of the profile was due to the temperature-dependent offset of the inclinometer. For the profile in the wPO, the VMP-X was ballasted to be slightly denser, and it fell at 0.78 m s^{-1} (Fig. 6b, gold) and slowed to 0.75 m s^{-1} near the bottom. The profiler accelerated considerably in the first 500 m of its flight, possibly due to the compression of air trapped in its floodable cavities. When the VMP-X was 180 m above the bottom, it slowed rapidly by 0.03 m s^{-1} for unknown reasons, quickly settled to a speed of 0.73 m s^{-1}, and accelerated back to 0.75 m s^{-1} in the final 50 m of its flight. The pitch was 1.7° (Fig. 6, green) and its fluctuations were similar to those in the sSCS.

For the profile in the wPO, there were many interruptions of communication between the MicroXM and the datalogger that are evident by the data gaps. This appears to be caused by pressure-induced stress on the unprotected fiber at its MicroXM end, does not occur in all units, and a solution is being pursued by the manufacturer. The transients of the fall rate (of magnitude 0.02 m s^{-1}) at the recommencement of communication are an artifact of the deconvolution algorithm used to compute the fall rate from the preemphasized pressure record. These transients bias the estimation of the local rate of dissipation by less than 10%.

b. *The rate of dissipation*

For the southern South China Sea, the microstructure shear (Fig. 7a) reported by both probes decreases with depth, is small below 1000 m, and is significant only

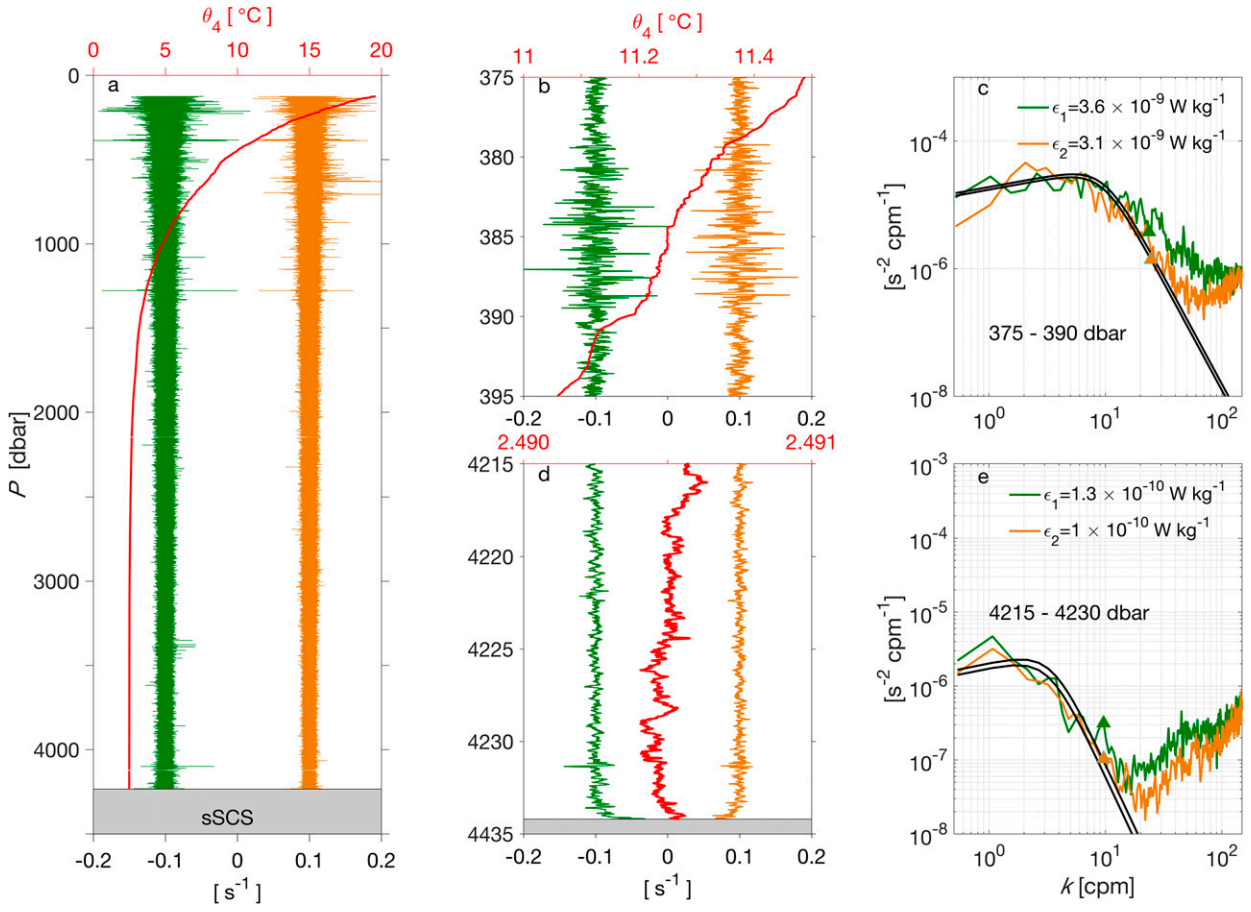

FIG. 7. Profiles of the microstructure shear from probe 1 (green, offset by −0.1) and probe 2 (gold, offset by 0.1), and the potential temperature relative to 4000 dbar (red) in the sSCS. (a) Full-depth view and (b),(d) selected depth ranges. The spectra of the shear for the pressure ranges (c) 375–390 and (e) 4215–4230 dbar. Triangles mark the limits of k_{max} in (1). Thick lines are the Nasmyth spectra for the estimated rates of dissipation for each probe. Gray shading identifies the bottom.

intermittently in shallower water (Fig. 7b). In the stably stratified depth range of 375–395 dbar, the amplitude of shear rose above its typical value of 0.02 to reach 0.1 s^{-1}. The spectrum of shear (Fig. 7c) follows the Nasmyth spectrum (Nasmyth 1970; Oakey 1982; Wolk et al. 2002) closely up to 40 cycles per meter (cpm). Near the bottom, the amplitude of shear fluctuations is typically 0.01 s^{-1} (Fig. 7d), and the spectrum of shear follows the Nasmyth spectrum up to about 20 cpm (Fig. 7e). The meter-scale fluctuations of temperature near the bottom are smaller than 100 μK.

The rate of dissipation of kinetic energy ε in isotropic turbulence is defined as

$$\varepsilon = \frac{15}{2}\nu\overline{\left(\frac{\partial u}{\partial z}\right)^2} = \frac{15}{2}\nu\int_0^{k_{max}}\psi(k)\,dk, \qquad (1)$$

where ν is the kinematic molecular viscosity, the overline indicates a spatial average, u is either one of the two horizontal components of velocity, z is the vertical coordinate, $\psi(k)$ is the spectrum of the vertical shear, and k is the vertical wavenumber (Osborn 1980). The upper limit of integration k_{max} is variable. It is the smallest of the following values: (i) the lowest frequency that shows corruption of the shear signal by vibrations; (ii) the wavenumber of 150 cpm due to the spatial resolution of the shear probe; (iii) the cutoff frequency of the anti-aliasing filter; (iv) an estimate of the wavenumber that resolves 90% of the shear variance according to the Nasmyth spectrum, using the method of Lueck (2013); and (v) the location of the spectral minimum determined with a low-order fit to the spectrum in log–log space.

The estimated rates of dissipation in the sSCS, for the depth interval of 375–390 dbar (Fig. 7c), using (1), are $\varepsilon_1 = 3.6\times10^{-9}$ and $\varepsilon_2 = 3.1\times10^{-9}$ W kg^{-1} for probes 1 and 2, respectively. For the bottom 15 dbar of this profile, the rates are 1.3×10^{-10} and 1.0×10^{-10} W kg^{-1}

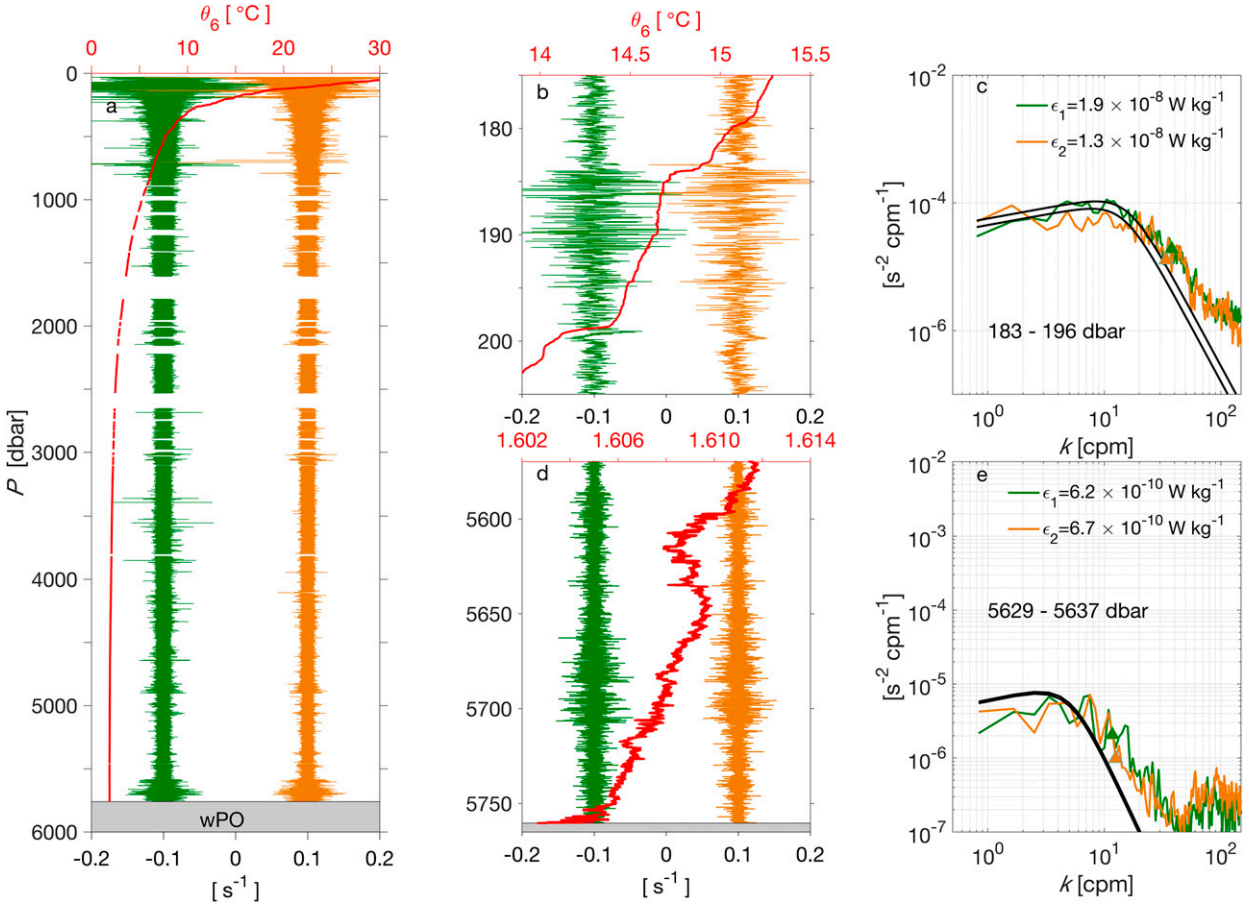

FIG. 8. As in Fig. 7, but for the wPO.

(Fig. 7e). For these figures, the potential temperature relative to 4000 dbar, θ_4, was estimated using a salinity of 34.7 psu and a pressure-dependent correction of 0.97×10^{-4} K dbar^{-1} (section 3e) to adjust the temperature readings because the thermistor is not protected from the ambient pressure.

For the western Pacific Ocean, where the bottom is comparably rougher, the vertical profile of shear is similar to that in the sSCS except within 200 m of the bottom (Fig. 8a), where the amplitude of the shear fluctuations reach 0.1 s^{-1} peak to peak. The thermocline has numerous $O(10)$ m vertical-scale patches of turbulence (Fig. 8b) that mix the stably stratified waters. The spectra of shear (Fig. 8c) in these layers follow the Nasmyth spectrum up to about 30 cpm. In the bottom layer (Fig. 8d), shear variance peaks 75 m above the bottom. The potential temperature profile is irregular, contains several inversions at scales larger than 1 m, and the meter-scale fluctuations are 2 mK. The gradient of potential temperature is, on average, positive. The rates of dissipation from the two shear probes are 6.2×10^{-10} and 6.7×10^{-10} W kg^{-1} (Fig. 8e), in the underside of the large ~2-mK inversion at 5630 dbar. The depth range of the near-bottom turbulence is the same as the range of fall speed anomaly (Fig. 6).

c. *Dissipation noise*

The typical noise level of the VMP-X is well below 1×10^{-10} W kg^{-1} (Fig. 9). The shear signals have been high-pass filtered at 0.15 Hz (0.20 cpm) to permit a resolution of the low-wavenumber part of the shear spectrum. The Nasmyth spectrum for $\varepsilon = 3.5 \times 10^{-11}$ W kg^{-1} (black line) agrees with the measured spectra up to approximately 8 cpm. The band from 20 to 200 cpm is dominated by vibrations induced by the drag brushes. The spectrum drops steeply for higher wavenumbers due to the antialiasing filters, which are set to 150 Hz. Above 400 cpm the spectra level out to the sampling noise floor. The spectra of Fig. 9 have not been corrected for the wavenumber response of the shear probe (Macoun and Lueck 2004). Applying this correction boosts the spectra by a factor of 2 at 48 cpm.

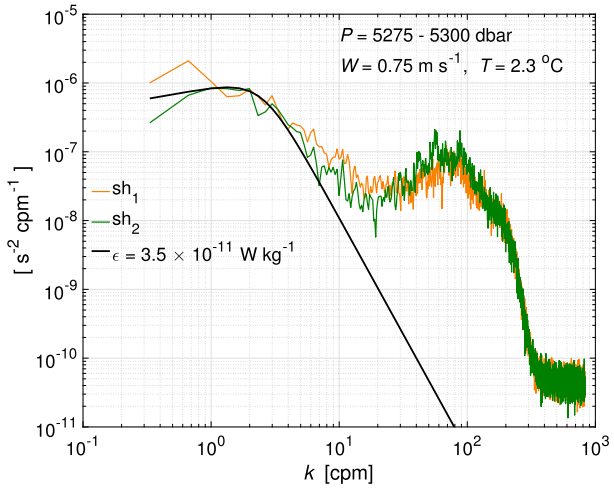

FIG. 9. Spectra of shear for probe 1 (green) and probe 2 (gold) for the pressure range of 5275–5300 dbar in the wPO. Black line is the Nasmyth spectrum for $\varepsilon = 3.5 \times 10^{-11}$ W kg^{-1}.

d. Bottom impact

The main objective of the development of the VMP-X is profiling right to the bottom to study the benthic boundary layer. Damaging the MicroXM is not an issue because it is not recovered. Hard bottoms are not a problem for the recovery of the VMP-X. However, soft mud may allow a penetration of the MicroXM and the lower part of the VMP-X vehicle, and this could delay the release of the MicroXM. Very fine mud is common in the sSCS and the instrument did penetrate the bottom (Fig. 10a). The pressure increases linearly until $t = 8336$ s. The pressure jumps by 2.6 dbar and then rapidly rebounds to a pressure that is 0.6 dbar higher than the pressure at the moment of contact with the bottom. If we assign a density of 1500 kg m^{-3} to the mud (Hamilton 1976), then the penetration into the mud is about $D = 0.4$ m. The pressure sensed during the impact is a combination of the hydrostatic pressure and the pressure on the front face of the MicroXM that is required to decelerate the vehicle. The deceleration is approximately

$$a = \frac{W^2}{2D} = 0.41 \text{ m s}^{-2}, \tag{2}$$

where $W = 0.57$ m s^{-1} is the fall rate of the VMP-X. The mass of the vehicle is the sum of its true mass (60 kg), plus the mass of water within its freely flooding tube (~10 kg), plus the mass of water entrained around the outside of the vehicle (~40 kg). The combined total is approximately 110 kg. The average force during the bottom impact, F, is the product of the mass and acceleration and equals approximately 55 N. If this force is generated by the excess pressure over the front face of the MicroXM, then this pressure is

$$\delta P = \frac{4F}{\pi d^2} = 0.57 \times 10^4 \text{ Pa} = 0.57 \text{ dbar}, \tag{3}$$

where $d = 0.1$ m is the diameter of the MicroXM. The peak anomaly of the pressure signal is 2 dbar (Fig. 10a).

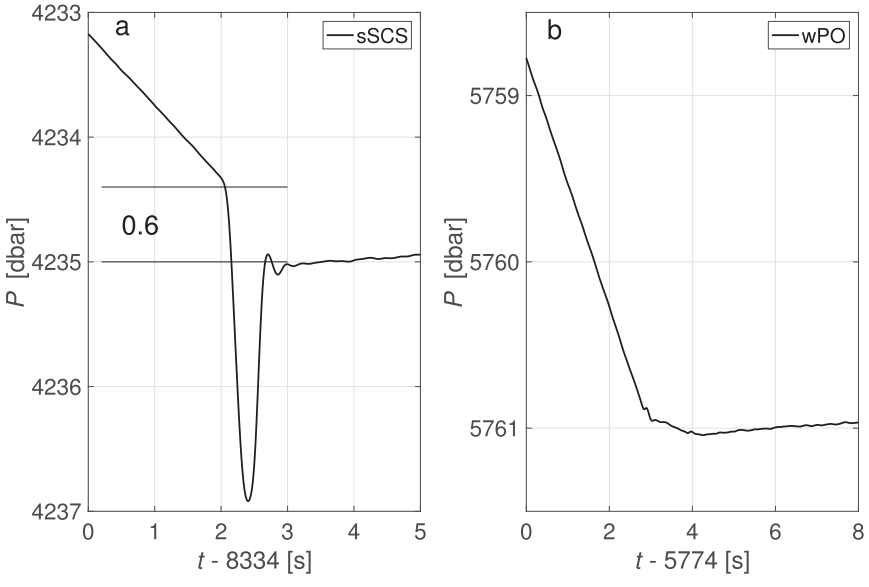

FIG. 10. Pressure record during the impact of the VMP-X on a (a) soft and (b) hard bottom in the sSCS and wPO, respectively. Time offset from the start of each profile is indicated in the axis label.

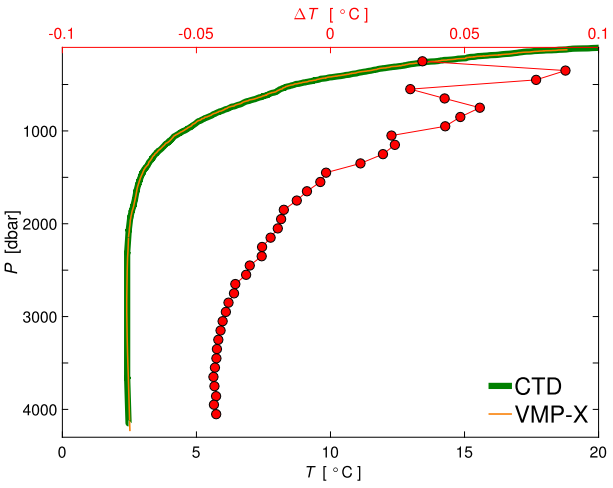

FIG. 11. Profile of temperature collected with a CTD (green) and the VMP-X (gold) for the sSCS, and their difference, $\Delta T = T_{\mathrm{CTD}} - T_{\mathrm{VMP-X}}$, averaged over intervals of 100 dbar (red circles).

The average of the pressure pulse is 1 dbar and is roughly consistent with this simple model of bottom impact. The postimpact signals from the shear probes indicate that they were not broken. Data were recorded for an additional 45 min, which means that the VMP-X was stuck in the mud for that duration, because the burn wire release typically frees the MicroXM in less than 2 min.

An impact with a hard bottom shows a very different pressure record (Fig. 10b). The rate of change of pressure decreases significantly during $5777 < t < 5778$ s and then becomes slightly negative. Both shear probes were destroyed immediately by the impact. The pressure record is consistent with an elastic deformation of the rubber coupler that connects the MicroXM to the vehicle. The data ended 3 min after impact, which must be the time it took the burn wire to free the MicroXM.

e. *Temperature accuracy*

The temperature sensor on the MicroXM is not protected from the hydrostatic pressure of seawater. Applying pressure to a thermistor reduces its resistance and causes it to read high. The temperature readings have been adjusted using

$$T = T_0 - \gamma P, \tag{4}$$

where T_0 is the temperature derived from the calibration conducted at atmospheric pressure, P is the in situ pressure, and $\gamma = 0.97 \times 10^{-4}\,\mathrm{K\,dbar^{-1}}$ is the pressure coefficient of the thermistor. The pressure-adjusted temperature reported by the VMP-X agrees well with the values reported by a nearly concurrently deployed CTD (Fig. 11). The value of γ was chosen to minimize the variations of the temperature difference with respect to pressure for pressures greater than 2000 dbar. The temperature difference for shallower depths is mainly due to the deviations of a linear Steinhart–Hart equation (section 2d), the displacement of isotherms by internal waves, and the error of a first-order calibration of the pressure transducer. For example, the large-scale temperature gradient above 1000 m is approximately $1.5 \times 10^{-2}\,^{\circ}\mathrm{C\,m^{-1}}$. A depth error, or isotherm displacement of 10 m, can induce a difference of 0.15°C between the temperature reported by the two instruments. The start of the CTD cast and the VMP-X deployment were separated in time and space by 16 min and 125 m, respectively.

4. Analysis

Profiles of ε and the squared buoyancy frequency N^2 will be used to compare the diapycnal diffusivity in the sSCS (Fig. 12) against that in the wPO (Fig. 13). The square of the buoyancy frequency is computed using $N^2 = -g/\rho\partial\rho_\theta/\partial z$, where ρ_θ is the potential density obtained from nearly concurrent CTD casts. The square of the vertical shear is derived using $S^2 = (\partial U/\partial z)^2 + (\partial V/\partial z)^2$, where the velocity components are obtained from the LADCP. All parameters are averaged into 50-m bins. The diapycnal diffusivity is estimated using $\kappa = 0.2\varepsilon/N^2$ (Osborn 1980).

For both locations, the rate of dissipation decreases with increasing depth, from $\varepsilon \sim 10^{-9}\,\mathrm{W\,kg^{-1}}$ near a depth of 500 m to $\varepsilon \sim 3 \times 10^{-11}\,\mathrm{W\,kg^{-1}}$ below the depth of 2000 m. In the sSCS the bathymetry is smooth and changes by only a few tens of meters within a radius of 30 km around the location of this profile. Even so, there is a slight elevation of ε within 150 m of the bottom (Fig. 12a). The mean-square vertical shear is typically $1 \times 10^{-5}\,\mathrm{s^{-2}}$ below the depth of 1000 m (Fig. 12d). The smooth topography, small shear, weak tidal energy (Waterhouse et al. 2014; Shang et al. 2015), and absence of internal waves at the low latitude of this profile (Gregg et al. 2003) combine to produce an environment of low-intensity microstructure in the deeper waters at this station. The diapycnal diffusivity κ increases with increasing depth (Fig. 12b). The diffusivity is less than $10^{-5}\,\mathrm{m^2\,s^{-1}}$ above 1000-m depth and increases to $\sim 10^{-4}\,\mathrm{m^2\,s^{-1}}$ below 3500 m. The depth variation of κ is mainly due to the depth variation of N^2.

In the wPO, the profile of ε is similar to the profile in the sSCS except that it is punctuated by several distinct layers of enhanced dissipation and is it much more variable below the depth of 4000 m (Fig. 13a). The most distinct feature is the factor of 100 increase of ε within 200 m of the bottom. The bathymetry is decidedly much rougher in the wPO compared to the sSCS. The bottom

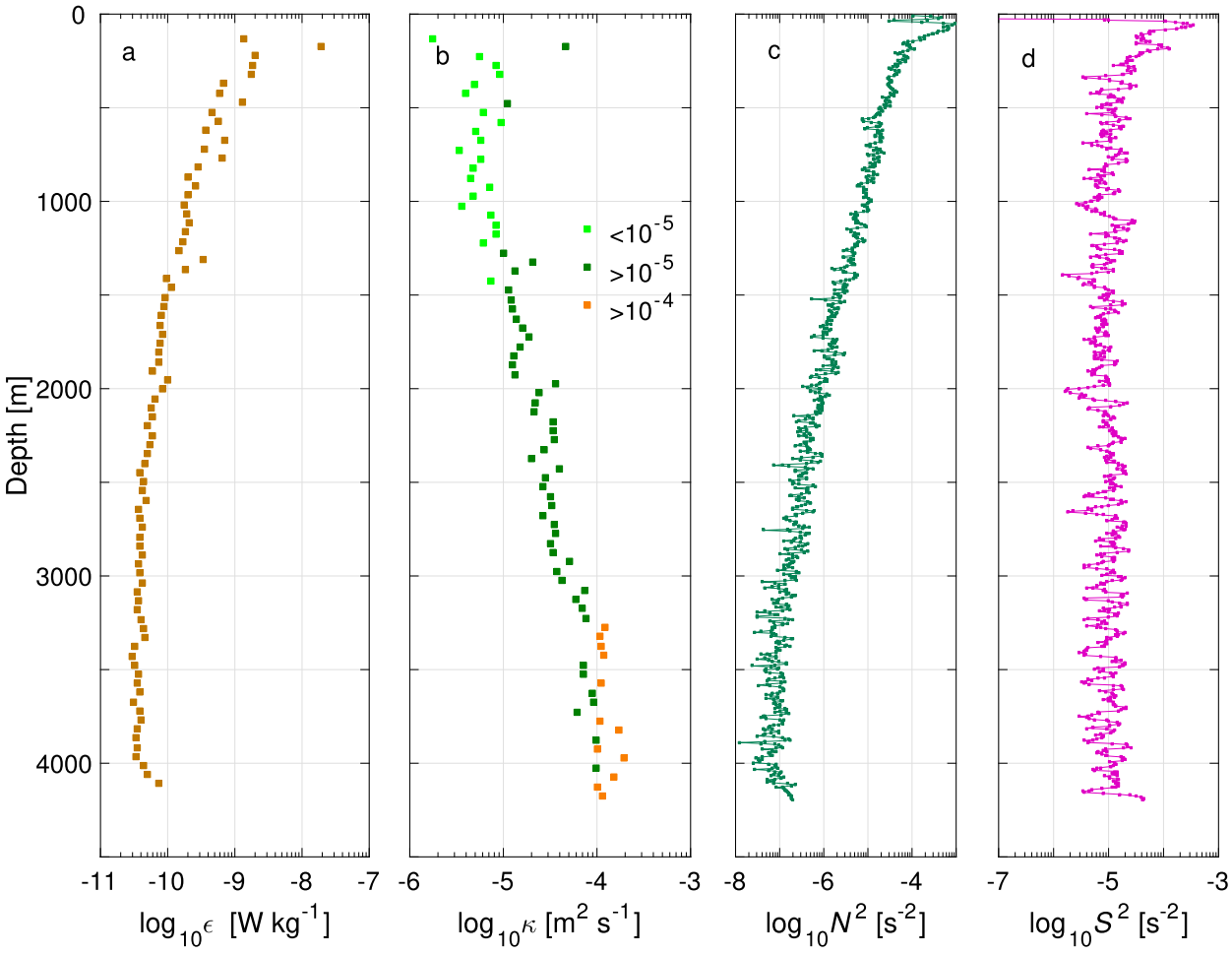

FIG. 12. Profiles of the rate of dissipation ε from (a) both probes, (b) the diapycnal eddy diffusivity κ, (c) the square of the buoyancy frequency N^2, and (d) the square of the vertical shear S^2, averaged into 50-m bins, for the sSCS.

depth varies from 3720 to 7950 m within a radius of 30 km around the site of this profile. The mean-square shear (Fig. 13d) increases with depth below 1000 m and reaches $\sim 1 \times 10^{-4}\,\mathrm{s}^{-2}$ near the bottom, a values that is 10 times larger than in the sSCS. The squared buoyancy frequency (Fig. 13c) decreases with depth but less steeply than in the sSCS, and N^2 never fully declines to $1 \times 10^{-7}\,\mathrm{s}^{-2}$. The diapycnal diffusivity (Fig. 13b) increases with depth, has elevated values in the layers of elevated dissipation, and grows steeply to $5 \times 10^{-3}\,\mathrm{m}^2\,\mathrm{s}^{-1}$ in the turbulent layer that is 250 m above the bottom. The diapycnal diffusivity, averaged over all depth, is 0.9×10^{-4} and $0.3 \times 10^{-4}\,\mathrm{m}^2\,\mathrm{s}^{-1}$ in the wPO and sSCS, respectively.

Previous microstructure measurements (Hibiya et al. 2007) have revealed a latitudinal dependence of the diapycnal diffusivity that is incorporated into most finescale parameterizations (Hibiya and Nagasawa 2004; Kunze et al. 2006), with lower diffusivity at lower latitude because of the reduced mixing from the breaking of internal waves in equatorial waters (Gregg et al. 2003). Using finescale measurements, Kunze et al. (2006) inferred a diffusivity ranging from $0.03 \times 10^{-4}\,\mathrm{m}^2\,\mathrm{s}^{-1}$ within 2° of the equator to $\approx 0.5 \times 10^{-4}\,\mathrm{m}^2\,\mathrm{s}^{-1}$ at latitudes of 50°–70°N, and a value of less than $0.1 \times 10^{-4}\,\mathrm{m}^2\,\mathrm{s}^{-1}$ at 11°N. The microstructure measurements of Hibiya et al. (2007) indicate a diffusivity of less than $0.1 \times 10^{-4}\,\mathrm{m}^2\,\mathrm{s}^{-1}$ in the main thermocline of the Pacific at 11°N. Our results show a much larger diffusivity when we incorporate the contribution of the near-bottom boundary layer. Even over smooth bathymetry, such as in the southern South China Sea, the diffusivity is 3 times larger than the values in previous reports that excluded the bottom layer.

5. Summary

VMP-X was designed to supplement conventional vertical microstructure profilers (Lueck et al. 2002) for situations where a conventional instrument may be

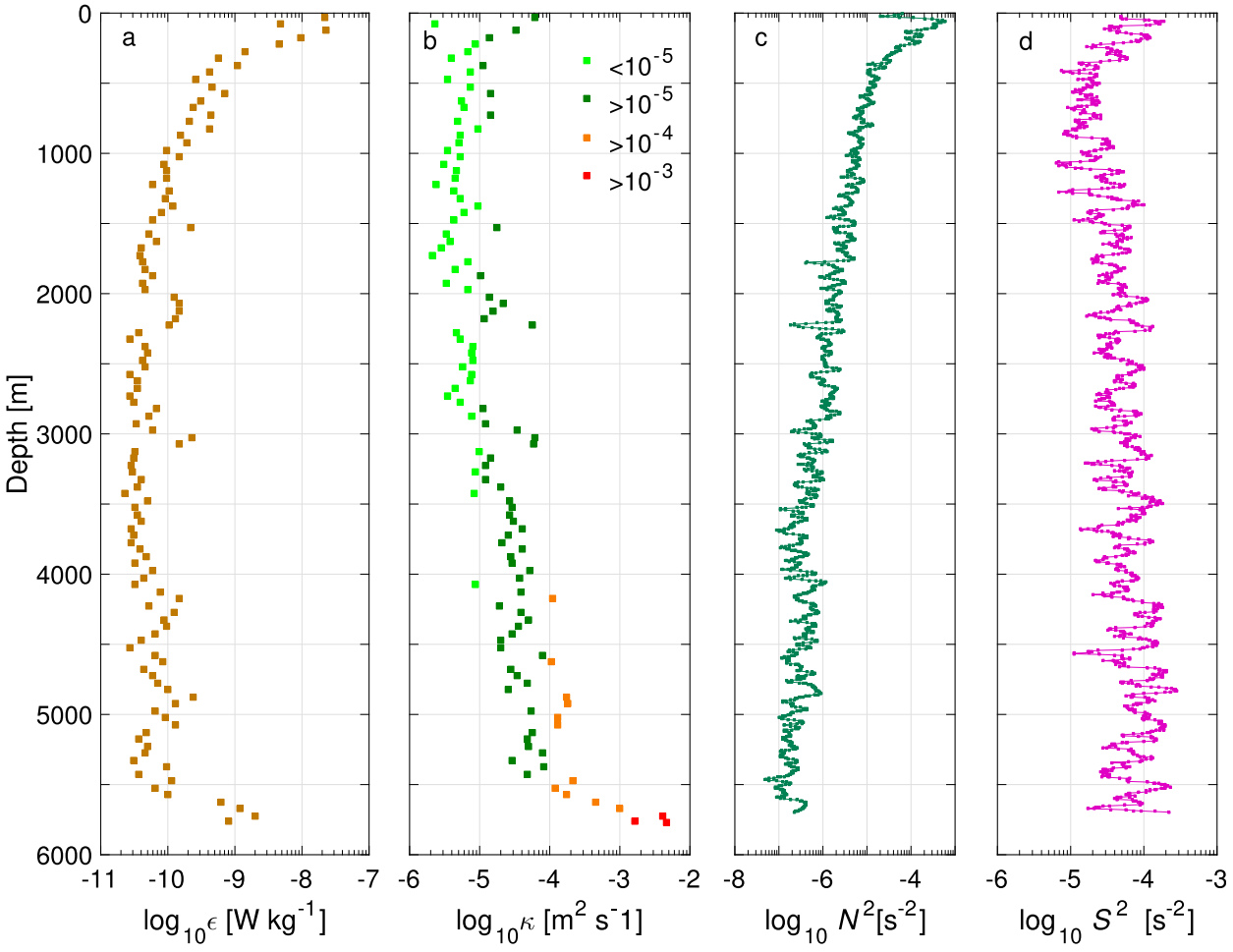

FIG. 13. As in Fig. 12, but for the wPO.

unsuitable or unacceptably risky, such as profiling through the entire benthic boundary layer. Deep ocean profiles require extremely low noise measurements. The VMP-X achieves noise levels (3×10^{-11} W kg^{-1}) that are comparable with larger instruments, even though it is partially expendable. However, the MicroXM is nonconfigurable and can be used only for one deployment. It has the potential to significantly increase the amount of data collected in the deep near-bottom layers of the ocean.

The VMP-X has been used to demonstrate, that near-bottom turbulence is enhanced relative to large distances above the bottom, and that this enhancement is much larger over rough bathymetry than it is over smooth bathymetry, using a pair of profiles collected at similar latitudes in the southern South China Sea (11°N) and in the western North Pacific Ocean (12°N). The 6000-m depth rating of the VMP-X has enabled us to estimate the diapycnal diffusivity over the entire water column to show that bottom mixing can make a large contribution to the depth-average diffusivity, and that this average may be close to the canonical value of 1×10^{-4} m^2 s^{-1} that is required to balance the vertical advection of heat due to the production of bottom water at high latitudes.

Acknowledgments. We thank the captain and crew of the R/Vs *Shiyan 3* and *Kexue* for their assistance with the deployment of the VMP-X. We also appreciate the help of scientists from the South China Sea Institute of Oceanology and the Institute of Oceanology, CAS. This work is supported by the Special Fund for Strategic Leading Science and Technology from the Chinese Academy of Sciences (Grant XDA11010202) and the National Natural Science Foundation of China (Grants 41630970, 41376022, 41276021, and 41521005).

REFERENCES

Fricker, D., and H. M. Nepf, 2000: Bathymetry, stratification, and internal seiche structure. *J. Geophys. Res.*, **105**, 14 237–14 251, doi:10.1029/2000JC900060.

Garrett, C., 2003: Internal tides and ocean mixing. *Science*, **301**, 1858–1859, doi:10.1126/science.1090002.

Gregg, M. C., 1989: Scaling turbulent dissipation in the thermocline. *J. Geophys. Res.*, **94**, 9686–9698, doi:10.1029/JC094iC07p09686.

——, T. B. Sanford, and D. P. Winkel, 2003: Reduced mixing from the breaking of internal waves in equatorial waters. *Nature*, **422**, 513–515, doi:10.1038/nature01507.

Hamilton, E. L., 1976: Variations of density and porosity with depth in deep-sea sediments. *J. Sediment. Res.*, **46**, 280–300, doi:10.1306/212F6F3C-2B24-11D7-8648000102C1865D.

Hibiya, T., and M. Nagasawa, 2004: Latitudinal dependence of diapycnal diffusivity in the thermocline estimated using a finescale parameterization. *Geophys. Res. Lett.*, **31**, L01301, doi:10.1029/2003GL017998.

——, ——, and Y. Niwa, 2007: Latitudinal dependence of diapycnal diffusivity in the thermocline observed using a microstructure profiler. *Geophys. Res. Lett.*, **34**, L24602, doi:10.1029/2007GL032323.

Kunze, E., E. Firing, J. M. Hummon, T. K. Chereskin, and A. M. Thurnherr, 2006: Global abyssal mixing inferred from lowered ADCP shear and CTD strain profiles. *J. Phys. Oceanogr.*, **36**, 1553–1576, doi:10.1175/JPO2926.1.

Ledwell, J. R., and B. M. Hickey, 1995: Evidence for enhanced boundary mixing in Santa Monica Basin. *J. Geophys. Res.*, **100**, 20 665–20 679, doi:10.1029/94JC01182.

——, E. T. Montgomery, K. L. Polzin, L. C. St. Laurent, R. W. Schmitt, and J. M. Toole, 2000: Evidence for enhanced mixing over rough topography in the abyssal ocean. *Nature*, **403**, 179–182, doi:10.1038/35003164.

Lentz, S. J., and J. H. Trowbridge, 1991: The bottom boundary layer over the northern California shelf. *J. Phys. Oceanogr.*, **21**, 1186–1201, doi:10.1175/1520-0485(1991)021<1186:TBBLOT>2.0.CO;2.

Lorke, A. F., F. Peeters, and A. Wuest, 2005: Shear-induced convective mixing in the bottom boundary layers on slopes. *Limnol. Oceanogr.*, **50**, 1612–1619, doi:10.4319/lo.2005.50.5.1612.

Lueck, R. G., 2013: Calculating the rate of dissipation of turbulent kinetic energy. Rockland Scientific International Tech. Note TN-028, 18 pp. [Available online at http://rocklandscientific.com/?wpdmdl=1034.]

——, and T. D. Mudge, 1997: Topographically induced mixing around a shallow seamount. *Science*, **276**, 1831–1833, doi:10.1126/science.276.5320.1831.

——, F. Wolk, and H. Yamazaki, 2002: Oceanic velocity microstructure measurements in the 20th century. *Japan J. Oceanogr.*, **58**, 153–174, doi:10.1023/A:1015837020019.

Macoun, P., and R. Lueck, 2004: Modelling the spatial response of the airfoil shear probe using different sized probes. *J. Atmos. Oceanic Technol.*, **21**, 284–297, doi:10.1175/1520-0426(2004)021<0284:MTSROT>2.0.CO;2.

Mashayek, A., R. Ferrari, M. Nikurashin, and W. R. Peltier, 2015: Influence of enhanced abyssal diapycnal mixing on stratification and the ocean overturning circulation. *J. Phys. Oceanogr.*, **45**, 2580–2597, doi:10.1175/JPO-D-15-0039.1.

Moum, J. N., and R. G. Lueck, 1985: Causes and implications of noise in oceanic dissipation measurements. *Deep-Sea Res.*, **32A**, 379–390, doi:10.1016/0198-0149(85)90086-X.

Munk, W. H., 1966: Abyssal recipes. *Deep-Sea Res. Oceanogr. Abstr.*, **13**, 707–730, doi:10.1016/0011-7471(66)90602-4.

Nasmyth, P. W., 1970: Ocean turbulence. Ph.D. thesis, University of British Columbia, 69 pp.

Nikurashin, M., and R. Ferrari, 2010: Radiation and dissipation of internal waves generated by geostrophic motions impinging on small-scale topography: Application to the Southern Ocean. *J. Phys. Oceanogr.*, **40**, 2025–2042, doi:10.1175/2010JPO4315.1.

Oakey, N. S., 1982: Determination of the rate of dissipation of turbulent kinetic energy from simultaneous temperature and velocity shear microstructure measurements. *J. Phys. Oceanogr.*, **12**, 256–271, doi:10.1175/1520-0485(1982)012<0256:DOTROD>2.0.CO;2.

Osborn, T. R., 1980: Estimates of the local rate of vertical diffusion from dissipation measurements. *J. Phys. Oceanogr.*, **10**, 83–89, doi:10.1175/1520-0485(1980)010<0083:EOTLRO>2.0.CO;2.

——, and W. R. Crawford, 1980: An airfoil probe for measuring turbulent velocity fluctuations in water. *Air-Sea Interaction: Instruments and Methods*, F. W. Dobson, L. Hasse, and R. Davis, Eds., Plenum Press, 369–386.

Polzin, K. L., J. M. Toole, J. R. Ledwell, and R. W. Schmitt, 1997: Spatial variability of turbulent mixing in the abyssal ocean. *Science*, **276**, 93–96, doi:10.1126/science.276.5309.93.

Rye, C. D., M.-J. Messias, J. R. Ledwell, A. J. Watson, A. Brousseau, and B. A. King, 2012: Diapycnal diffusivities from a tracer release experiment in the deep sea, integrated over 13 years. *Geophys. Res. Lett.*, **39**, L04603, doi:10.1029/2011GL050294.

Shang, X., Q. Liu, X. Xie, G. Chen, and R. Chen, 2015: Characteristics and seasonal variability of internal tides in the southern South China Sea. *Deep-Sea Res. I*, **98**, 43–52, doi:10.1016/j.dsr.2014.12.005.

Sommer, T., J. R. Carpenter, M. Schmid, R. Lueck, and A. Wueest, 2013: Revisiting microstructure sensor responses with implications for double-diffusive fluxes. *J. Atmos. Oceanic Technol.*, **30**, 1907–1923, doi:10.1175/JTECH-D-12-00272.1.

Steinhart, J. S., and S. Hart, 1968: Calibration curves for thermistors. *Deep-Sea Res. Oceanogr. Abstr.*, **15**, 497–503, doi:10.1016/0011-7471(68)90057-0.

St. Laurent, L., A. C. Naveira Garabato, J. R. Ledwell, A. M. Thurnherr, and J. M. Toole, 2012: Turbulence and diapycnal mixing in Drake Passage. *J. Phys. Oceanogr.*, **42**, 2143–2152, doi:10.1175/JPO-D-12-027.1.

Thorpe, S. A., 1997: On the interactions of internal waves reflecting from slopes. *J. Phys. Oceanogr.*, **27**, 2072–2078, doi:10.1175/1520-0485(1997)027<2072:OTIOIW>2.0.CO;2.

Toole, J. M., K. L. Polzin, and R. W. Schmitt, 1994: Estimates of diapycnal mixing in the abyssal ocean. *Science*, **264**, 1120–1123, doi:10.1126/science.264.5162.1120.

Waterhouse, A. F., and Coauthors, 2014: Global patterns of diapycnal mixing from measurements of the turbulent dissipation rate. *J. Phys. Oceanogr.*, **44**, 1854–1872, doi:10.1175/JPO-D-13-0104.1.

Whalen, C. B., L. D. Talley, and J. A. MacKinnon, 2012: Spatial and temporal variability of global ocean mixing inferred from Argo profiles. *Geophys. Res. Lett.*, **39**, L18612, doi:10.1029/2012GL053196.

Wolk, F., H. Yamazaki, L. Seuront, and R. G. Lueck, 2002: A new free-fall profiler for measuring biophysical microstructure. *J. Atmos. Oceanic Technol.*, **19**, 780–793, doi:10.1175/1520-0426(2002)019<0780:ANFFPF>2.0.CO;2.

Wunsch, C., and R. Ferrari, 2004: Vertical mixing, energy, and the general circulation of the oceans. *Annu. Rev. Fluid Mech.*, **36**, 281–314, doi:10.1146/annurev.fluid.36.050802.122121.